

# CHARACTERIZING THE INFRARED SPECTRA OF SMALL, NEUTRAL, FULLY DEHYDROGENATED PAHS

C. J. MACKIE<sup>1,2</sup>, E. PEETERS<sup>1,3</sup>, C. W. BAUSCHLICHER, JR.<sup>4</sup>, AND J. CAMI<sup>1,3</sup>

*Accepted for publication in ApJ*

## ABSTRACT

We present the results of a computational study to investigate the infrared spectroscopic properties of a large number of polycyclic aromatic hydrocarbon (PAH) molecules and their fully dehydrogenated counterparts. We constructed a database of fully optimized geometries for PAHs that is complete for eight or fewer fused benzene rings, thus containing 1550 PAHs and 805 fully dehydrogenated aromatics. A large fraction of the species in our database have clearly non-planar or curved geometries. For each species, we determined the frequencies and intensities of their normal modes using density functional theory calculations. Whereas most PAH spectra are fairly similar, the spectra of fully dehydrogenated aromatics are much more diverse. Nevertheless, these fully dehydrogenated species show characteristic emission features at  $5.2\mu\text{m}$ ,  $5.5\mu\text{m}$  and  $10.6\mu\text{m}$ ; at longer wavelengths, there is a forest of emission features in the  $16\text{--}30\mu\text{m}$  range that appears as a structured continuum, but with a clear peak centered around  $19\mu\text{m}$ . We searched for these features in Spitzer-IRS spectra of various positions in the reflection nebula NGC 7023. We find a weak emission feature at  $10.68\mu\text{m}$  in all positions except that closest to the central star. We also find evidence for a weak  $19\mu\text{m}$  feature at all positions that is not likely due to  $\text{C}_{60}$ . We interpret these features as tentative evidence for the presence of a small population of fully dehydrogenated PAHs, and discuss our results in the framework of PAH photolysis and the formation of fullerenes.

*Subject headings:* astrochemistry – infrared:ISM – ISM:lines and bands – ISM:molecules – methods:numerical – molecular data

## 1. INTRODUCTION

The infrared (IR) spectra of almost all astronomical objects, ranging from young stellar objects to planetary nebulae, and from galactic nuclei to the general ISM of galaxies, are dominated by prominent emission bands at  $3.3$ ,  $6.2$ ,  $7.7$ ,  $8.6$ ,  $11.2$ ,  $12.7$ , and  $16.4\mu\text{m}$ , as well as weaker features at  $3.4$ ,  $3.5$ ,  $5.25$ ,  $5.75$ ,  $6.0$ ,  $6.9$ ,  $7.5$ ,  $10.5$ ,  $11.0$ ,  $13.5$ ,  $14.2$ ,  $17.4$ , and  $18.9\mu\text{m}$ . It has long been suggested (e.g. Leger & Puget 1984; Allamandola et al. 1985) that these bands are caused by the combined emission of a population of polycyclic aromatic hydrocarbon molecules (PAHs) with sizes of typically 50 C atoms. It is now generally accepted that this is indeed the case, and that PAHs lock up some 10–20% of the cosmic carbon (see e.g. Tielens 2008; Peeters 2014)<sup>5</sup>. Absorption of a single UV photon through an electronic transition, followed by internal energy redistribution, leaves PAHs in highly excited vibrational states. They then cool by fluorescence, emitting IR photons at the frequencies corresponding to these vibrational modes (Allamandola et al. 1989; Bakes & Tielens 1994; Bakes et al. 2001a,b). Since

some vibrational modes (in particular stretching or bending of C-C and C-H bonds) are common to most PAHs and also occur at similar frequencies, a population of PAHs will emit very strongly at those common frequencies. As a consequence, the observed emission bands are overall fairly similar in appearance in different lines of sight, and these IR PAH bands (from now on simply referred to as the IR bands) can thus not be used to identify individual PAH species.

However, there are clear (albeit sometimes subtle) variations in the precise peak positions, line profiles and band intensity ratios of the IR bands in different astronomical sources or even spatially within extended sources. From a comparison to laboratory spectra and theoretical calculations, these variations can be understood as changes in the properties of the underlying PAH population such as charge state, precise chemical make-up or size (Peeters et al. 2002; Hony et al. 2001; van Dienenhoven et al. 2004; Hudgins et al. 2005; Cami 2011).

A full understanding of these variations and the further development of quantitative diagnostic tools depends on the availability of spectral properties for large subsets of PAH species. Experimentally obtained and theoretically calculated spectra of hundreds of PAH species have become more available in recent years (see e.g. the NASA Ames PAH database; Bauschlicher et al. 2010a; Boersma et al. 2014). Model fits using such collections of PAH spectral properties with calculated fluorescence spectra can reproduce the observed emission and their variations remarkably well (e.g. Allamandola et al. 1999; Cami 2011; Boersma et al. 2014). However, these databases are still highly biased and incomplete, and it is not immediately clear whether all astrophysically relevant subclasses are included.

Electronic address: mackie@strw.leidenuniv.nl

<sup>1</sup> Department of Physics and Astronomy, University of Western Ontario, London, ON N6A 3K7, Canada

<sup>2</sup> Leiden Observatory, Leiden University, PO Box 9513, NL-2300RA, Leiden, The Netherlands

<sup>3</sup> SETI Institute, 189 Bernardo Ave, Mountain View, CA 94043, United States

<sup>4</sup> NASA Ames Research Center, MS 245-6, Moffett Field, CA 94035, United States

<sup>5</sup> Note that over time, it has become clear that the astronomical emission does not correspond to PAHs as defined by the International Union of Pure and Applied Chemistry – i.e. only C and H – but rather to polycyclic aromatic compounds that can include hetero-atoms and substituted species or groups, correspond to various degrees of (de-)hydrogenation etcetera.

PAHs share many properties with another class of large aromatic species that was only recently detected in space. Cami et al. (2010) detected several emission bands (most notably at 7.0, 8.5, 17.4 and 18.9  $\mu\text{m}$ ) in the infrared spectrum of the peculiar planetary nebula Tc 1 and identified them with the vibrational modes of the fullerene species  $\text{C}_{60}$  and  $\text{C}_{70}$ . The characteristic  $\text{C}_{60}$  bands (especially the 17.4 and 18.9  $\mu\text{m}$  bands) have since been found in many objects, including several evolved stars (in our Milky Way galaxy as well as in the Magellanic Clouds; see e.g. García-Hernández et al. 2010, 2011a,b; Gielen et al. 2011; Zhang & Kwok 2011; Otsuka et al. 2013b,a) but also interstellar environments (Sellgren et al. 2010; Rubin et al. 2011; Peeters et al. 2012; Boersma et al. 2012) and young stellar objects (YSOs, Roberts et al. 2012). Of particular interest here is the spectrum of the Reflection Nebula (RN) NGC 7023. Sellgren et al. (2007) first suggested  $\text{C}_{60}$  as a possible carrier for the band at 18.9  $\mu\text{m}$  in this source; they later searched and detected also the 7.0  $\mu\text{m}$  band (Sellgren et al. 2010). Furthermore, near the central star, Berné et al. (2013) found several weak bands that are coincident with the vibrational modes of  $\text{C}_{60}^+$ .

One important aspect about cosmic fullerenes that is not understood yet is their precise formation route. Laboratory experiments have shown that fullerenes can self-assemble from a hot carbon vapour in a bottom-up process (Kroto et al. 1985; Jäger et al. 2009; Dunk et al. 2012, 2013). However, densities and temperatures in the circumstellar environments where fullerenes have been detected are generally too low for such a bottom-up route to complete in reasonable timescales. But other routes may exist as well. Chuvilin et al. (2010) showed that a graphene sheet rolls up and forms  $\text{C}_{60}$  molecules after losing an edge carbon atom. Based on these results, Berné & Tielens (2012) suggested that in space, similar processes may convert large PAHs into fullerenes. They argue that UV irradiation first results in fully dehydrogenated PAHs (which we refer to here as dPAHs<sup>6</sup>) and subsequently causes carbon loss which results in the formation of a pentagonal ring that induces curving up of the structure. Through isomerization the dPAH then rearranges to finally arrive at the very stable fullerene configuration on very short timescales. While such a formation route could be at play in RNe such as NGC 7023 where large PAHs could be abundantly available as starting materials, it is probably not the dominant route in PNe where we see fullerenes exclusively in the low-excitation objects (Otsuka et al. 2013a; Cami 2013; Sloan et al. 2014). In those environments, fullerenes could maybe form through aggregation and closed network growth (Dunk et al. 2012) from carbon clusters such as small dPAHs (Cami 2013). Alternative photoprocessing routes starting from Hydrogenated Amorphous Carbon (HAC) grains have been proposed as well (García-Hernández et al. 2010; Micelotta et al. 2012).

In either of the two formation routes starting from

<sup>6</sup> Even though fully dehydrogenated PAHs are technically speaking no longer considered a hydrocarbon, we still refer to these neutral dehydrogenated PAHs as dPAHs since they originate from the act of dehydrogenating PAHs in our exercise. Alternatives could be PAHs, PACs or graphene-like molecules.

PAHs, dPAHs are a clear intermediate step. Detecting the clear signatures of these dPAHs could thus further elucidate some of the pathways toward the processing and evolution of interstellar PAHs and the possible formation of fullerenes. However, as of yet, only a handful of individual dPAH species have been studied in great detail (see e.g. Bauschlicher & Ricca 2013), and it is thus not clear what (if any) could be a clear detection signature for the family of dPAHs as a whole. Consequently, it is not clear whether dPAHs are a component of the interstellar aromatic molecular species.

Here, we aim to characterize the changes in the infrared spectra of PAHs as they become fully dehydrogenated. To do this, we produced a comprehensive database of the structure and vibrational modes of PAH and dPAH species containing eight or fewer benzenoid rings. We used this database to study the spectral differences between PAHs and dPAHs, and to describe characteristic spectral features that could be indicative of the presence of dPAHs. Finally, we studied the Spitzer-IRS spectra of NGC 7023 at several positions between the PAH-dominated areas and the fullerene-rich zone to evaluate whether dPAHs could be present.

We present in § 2 the computational methods used to build the database. We present an overview of the resulting PAH and dPAH molecular structures in § 3 and the spectral analysis and characterization in § 4. Finally, the comparison between our calculated spectra and observations of NGC 7023 is presented in § 5.

## 2. COMPUTATIONAL METHODS

The goal of this work is to produce an unbiased database of the IR spectra of small PAHs and their dehydrogenated counterparts in order to characterize the changes to the spectra upon dehydrogenation. It was for this reason that we decided to produce a complete database of ever single possible PAH and corresponding dPAH species up to a given number of benzenoids. Other papers have looked at the effect on an IR spectrum of a PAH after removing all hydrogens, such as in Bauschlicher & Ricca (2013), but these only looked at a handful of species at a time. By studying a large and complete database of species, we can make better predictions of the dPAH family as a whole, and especially so for the subset of smaller dPAHs.

### 2.1. Enumerating PAH geometries

We used a recursive method to determine all possible PAH geometries. To produce all PAHs/dPAHs with  $h$  benzenoid members we add an additional benzenoid ring to each open edge of all species with  $h - 1$  benzenoids. Starting with a benzene seed we iterate this process up to species where  $h$  equals eight. To simplify the procedure each benzene ring is treated as a hexagon so that the problem becomes producing all possible simple polyhexes. The connectivity between each open face of each hexagon is then easily mapped by arranging them in a grid. After all  $h$  membered polyhexes are found a procedure then converts the vertexes of each hexagon to the coordinates representing the position of carbon atoms, adopting a C-C bond length at this point of 1.4 Å.

This method however produces duplicate species. To remove these duplicates each of the carbon skeletons

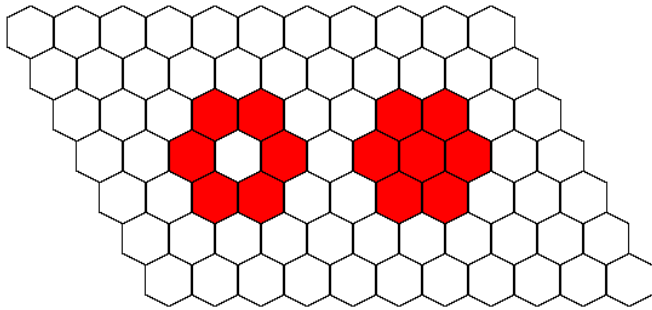


FIG. 1.— An illustration of our method to enumerate hexagons, and of the duplicates that arise when considering structures with a different number of hexagons. Shown in red on the left is a structure obtained by using 6 hexagons; on the right is a structure obtained using 7 hexagons. When considering only the vertices (i.e. the location of the carbon atoms), both structures are of course the same - the structure of coronene. Such issues arise starting from 5 benzenoid rings.

TABLE 1  
NUMBER OF PAH SPECIES WITH A NUMBER OF BENZENOID RINGS  
EQUAL TO  $h$

$h$	Dualist graph polyhexes	PAHs this paper
2	1	1
3	3	3
4	7	7
5	22	21
6	81	75
7	331	286
8	1436	1157
9	6510	4886
10	30129	20890

needs to be compared to the others with the same number of C atoms. We therefore calculated the moment of inertia tensor of each carbon skeleton, and used the resulting eigenvectors to produce a rotation matrix that rotates the species to lie along its principal axes. This causes each duplicate species to be rotated into the same orientation after which each coordinate of each carbon atom can be compared. It should be noted that reflections across axes also need to be compared as this method of rotating to the principal axes is ambiguous when it comes to direction of positive and negative directions. Moreover, if the moment of inertia is equal between two axes, we have to take axis interchangeability into account. After all duplicates are removed this method can be repeated using the outputted unique polyhexes as input for the next iteration.

Some ambiguity occurs though when  $h$  is equal to or greater than five, and is best illustrated by the situation depicted in Fig. 1. The two structures depicted in that figure are obtained for  $h = 6$  and  $h = 7$  respectively. However, since we are concerned with the hexagon *vertices* here (which correspond to the positions of the C atoms) and not the hexagon *faces*, both structures are identical for our purposes, and the  $h = 6$  structure really corresponds to 7 benzenoid rings. More generally, for  $h \geq 5$ , our method produces species out of  $h$  rings that we actually consider to be  $h+1$  membered rings; for  $h \geq 7$  we get species with  $h+2$  membered rings etcetera. Once all initial polyhexes are made the program then goes back and compares all species for uniqueness once again to check for duplicates across differing  $h$  numbers. For the

TABLE 2  
GROUND STATE SPIN STATE OF PAHs AND dPAHs

Spin state	% of total PAHs	% of total dPAHs
Singlet	54	27
Doublet	43	0
Triplet	3	37
Quadruplet	0	0
Quintet	0	28
Sextet	0	0
Septet	0	7
Octet	0	0
Nonet	0	1

sake of classifying these structures, the final number of benzenoid rings needs to be recounted. We assigned each duplicate species to the class corresponding to the highest number of benzenoids counted - e.g.  $h = 7$  for the example of coronene shown above.

We calculated all possible unique PAH structures for  $h \leq 10$  (see Table 1). It should be noted that the problem of enumerating all possible arrangements of a given number of adjoining hexagons has been investigated in mathematics using a method called the *dualist tree* (see e.g. Nikolić et al. 1990). However, the dualist tree method counts the *faces* of hexagons and not the vertices. Thus, what we consider to be duplicate PAH across differing  $h$  iterations are actually considered unique in the dualist tree method (see e.g. the coronene example in Fig. 1). Therefore the dualist tree method only sets an upper bound on the number of possible PAH structures for a given number of benzenoid rings, and thus the number of possible structures found in this paper are lower than the numbers predicted by the dualist tree method (Nikolić et al. 1990).

The polyhexes obtained in this way correspond to the initial geometries for the dPAHs. However, we will also need the geometries for the regular hydrogenated PAHs, i.e. we need to also determine the position of the H atoms. For our starting geometries, we used a simple computational technique that accurately places each hydrogen. Starting with the center of each hexagon the hydrogen atoms are placed radially out past each carbon atom. However, if a hydrogen atom ends up too close to a carbon atom as a result of this operation (such as in the body of a PAH), it is removed from the structure. This then results in the initial geometries for the regular PAHs.

## 2.2. Calculating spectral properties

We then computed the spectral properties of the PAHs and dPAHs using density functional theory (DFT). For all species, we used the Becke three-parameter, Lee-Yang-Parr (B3LYP) exchange-correlation functional (Becke 1993; Lee et al. 1988; Stephens et al. 1994) together with the 4-31G basis set (Frisch et al. 1984). The reliability of the B3LYP/4-31G approach has been considered several times previously in regards to PAHs. The average absolute and maximum errors in the scaled B3LYP/4-31G frequencies of naphthalene compared with experiment are 4.2 and 12.5  $\text{cm}^{-1}$ , respectively; these are to be compared with 2.8 and 8.1  $\text{cm}^{-1}$  for the very large cc-pVQZ basis set (Bauschlicher & Ricca 2010b). If the generalized gradient approximation is used instead of the hybrid B3LYP functional, the errors increase. A compar-

ison of the computed and experimental frequencies for 13 PAHs ranging in size from  $C_{22}H_{12}$  to  $C_{50}H_{22}$  again supported the use of the B3LYP/4-31G approach (Boersma et al. 2010). The scaled B3LYP/4-31G, B3LYP/6-31G\*, BP86/4-31G, and BP86/6-31G harmonic frequencies for  $C_{60}$  are in good mutual agreement and in good agreement with the 4 IR and 10 Raman bands from experiment (Bauschlicher 2014); the average absolute error for these four levels are 7.8, 4.2, 10.0, and 8.5  $cm^{-1}$ , respectively, while the maximum errors are 18.3, 12.9, 27.1, and 21.6  $cm^{-1}$ . This approach was also used for the majority of spectra in the NASA Ames PAH database Bauschlicher et al. (2010a); Boersma et al. (2014), and yields results that are accurate enough for our purposes, while not being too computationally expensive. All calculations were carried out using the software suite Gaussian 09 (Frisch et al. 2009).

We first formatted the atom coordinates of each PAH and dPAH for input into Gaussian 09. For each species, we then fully optimized the geometry, and subsequently calculated the harmonic vibrational frequencies. It has been shown that spin state can have an affect on line positions and intensities attributed to solo site electron pair interactions, and that the lowest spin state for dPAHs is not necessarily the ground state (Bauschlicher & Ricca 2013). Therefore, we also explored higher spin states for each PAH and dPAH molecule; due to the large number of species in our database however, we could only carry out the most basic test. Each species thus had its spin state increased; if this lowered the total energy (including the zero-point energy), we increased the spin state again until the spin state was found with the lowest energy. This was then taken as the ground state configuration. If a transition state was found it was disregarded, even though it is possible that geometry changes with higher spin states could result in lower energy. This had general affect of weakening the intensities of the bands between 5 and  $15\mu m$  by half relative to the intensities of the bands between 15 and  $30\mu m$ . No significant shifts in peak positions were observed. Table 2 summarizes the ground state spin states found for the PAHs and dPAHs. Note that neutral dPAHs always have an even number of electrons.

Although we calculated the initial structures for  $h \leq 10$ , we only calculated the spectra for all PAHs and dPAHs for  $h \leq 8$  due to computational limitations. One aspect that could not be fully automated was the process of producing optimized geometries, since any deviations from planarity (e.g. the repulsion due to two H atoms in close proximity) needed to be manually addressed. Moreover, when these deformations occur in multiple places on one particular species, an intuitive call about the stability of a particular stereochemistry has to be made.

Stability issues also lowered the number of corresponding dPAHs. We found that a PAH containing a linear chain of three or more benzenoids generally caused the structure of the corresponding dPAH to “explode” (see e.g. Fig. 2 for an example). Again, manual intervention was needed to detect and remove these species since Gaussian considered these species to be converged properly. These “exploded dPAHs” were not included in the database. The final database produced for this paper thus contains 1550 PAHs and 805 dPAHs. The largest of

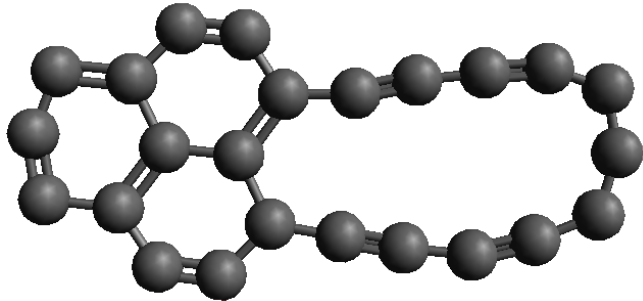


FIG. 2.— An example of the “exploding” dPAH structures that result from optimizing the geometry of species with three (or more) linearly arranged benzenoids.

TABLE 3  
FRACTIONS OF PAHs AND dPAHs IN THE DATABASE WITH A GIVEN FEATURE.

Property	% of total PAHs	% of total dPAHs
Planar	36	52
Non-planar	64	48
Radical	43	0
Non-radical	57	100
Odd #C	43	46
Even #C	57	54
Pericondensed	71	99
Catacondensed	29	1
Hexagons only	100	23
Pentagon containing	0	71
Quadrilateral containing	0	15

which contains 34 carbon atoms.

### 3. CONTENT OF THE DATABASE: MOLECULAR STRUCTURES

Our complete and unbiased database of all possible small PAHs and dPAHs (up to eight benzenoids) allows for a survey of the general geometries and structures of the family of PAHs. We studied various notable or interesting properties; a summary table of these results is given in Table 3.

In the process of optimizing the molecular geometries, we noticed that deviations from a purely planar structure are very common for PAHs. In fact, the majority of the PAHs and about half of the dPAHs were found to be non-planar. This is somewhat contrary to the typical representation in the literature of a PAH being represented as a planar species. We recognized two different geometric configurations that result in departures from planarity. First, we found that deep bay regions or “fjords” (as shown in Fig. 3) are very common; hydrogen-hydrogen repulsion in these fjords causes sometimes strong deformations. A second configuration involves pericondensed regions connected by catacondensed bridges, (see Fig. 3) which causes a very slight twisting of the molecule along the bridges. This slight twisting can be thought of as the two pericondensed regions repulsing each other. It should also be noted that some larger PAHs have multiple points of H-repulsion or bridge twisting; this then introduces stereochemistry in larger PAHs. For the work presented in this paper, it was assumed that the trans-twisting was lower in energy than the cis-bending of the geometries and therefore more important to the overall spectrum of a species.

About half of the dPAHs also turn out to be non-

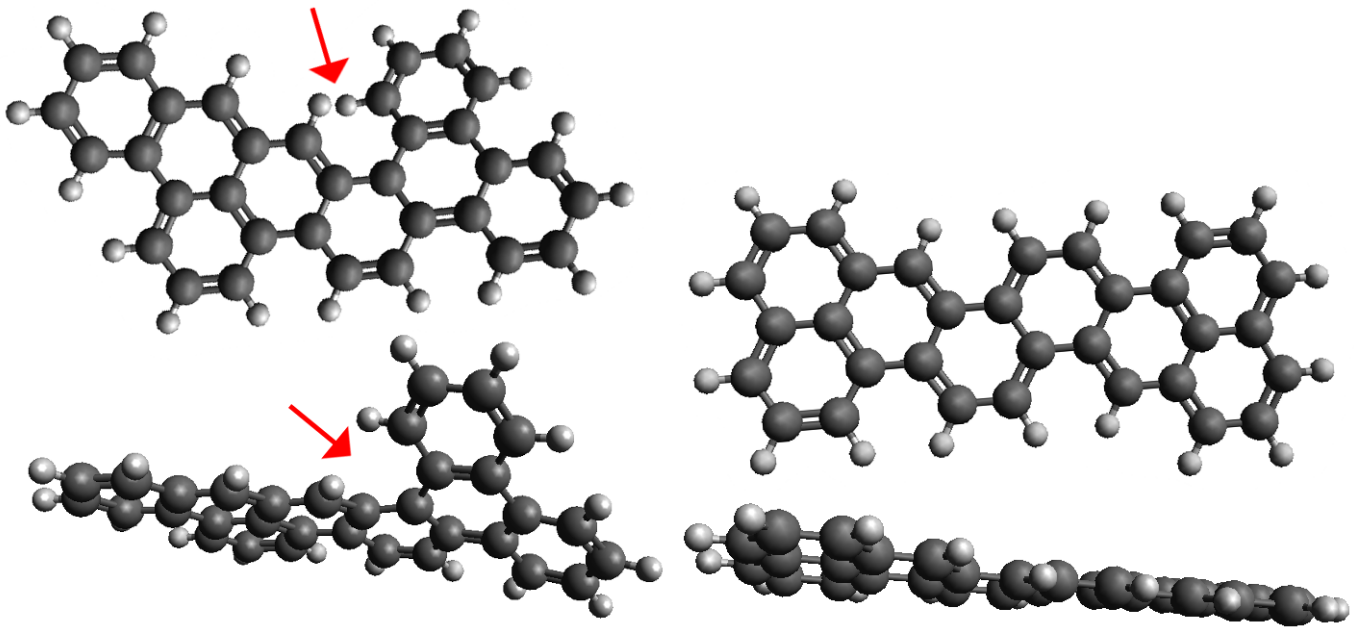


FIG. 3.— Two examples of deformations in PAH structures that lead to non-planarity. (*Left*) Top and side views of a “fjord” region (indicated by the red arrows) that results in a very strong deformation. (*right*) Top and side views of catacondensed bridges between pericondensed regions result in a slight twisting deformation.

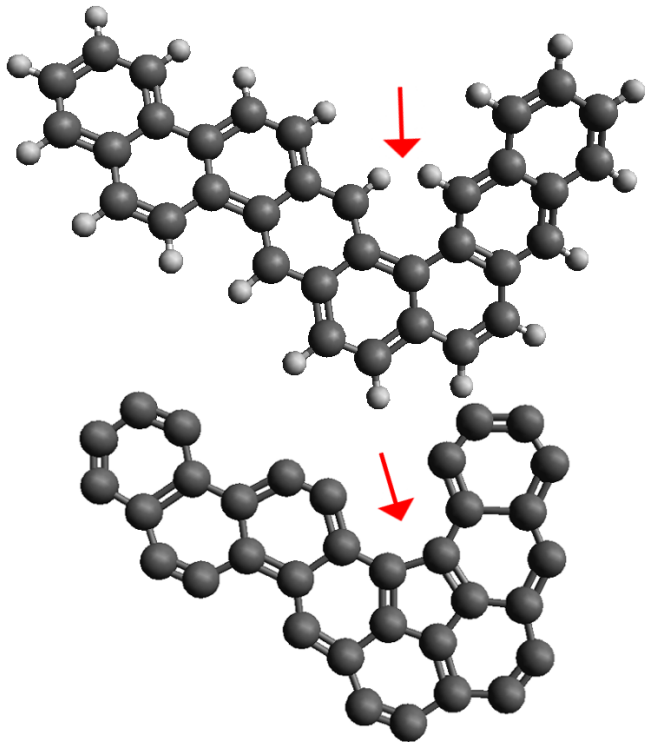


FIG. 4.— An example of the formation of pentagonal rings upon dehydrogenation of PAHs with fjord regions.

planar. For the dPAHs though, the departure from planarity is due to a different reason since no hydrogen atoms are available to repulse anymore. For dPAHs instead, it is the formation of pentagonal rings that causes the non-planarity. A typical example is shown in Fig. 4. When removing the hydrogen atoms of a regular PAH with a fjord region, the fjord region closes up into a pentagonal ring. The more these pentagons were central to the molecular structure, the more bowl-like the

dPAHs become. Note though that the formation of a pentagon does not always result in a non-planar species: as can be seen from Table 3, only 48% of the dPAHs are non-planar, whereas 71% contain at least one pentagon. Quadrilateral shapes (i.e. four-membered rings) also formed in some species, but always in conjunction with pentagon formation.

It is also interesting to note from Table 3 that there are very few ( $\sim 1\%$ ) catacondensed dPAH structures. This can be explained by two reasons. First, as stated earlier, dPAHs with linear structures are much less stable than clustered structures (see also the example of exploding PAHs in Fig. 2). The second reason is more subtle. When removing the hydrogen atoms from a catacondensed PAH species, often a pentagon forms which can turn the structure into a pericondensed species.

#### 4. IR SPECTRAL PROPERTIES OF DPAHS

##### 4.1. Calculating IR PAH and dPAH spectra

Our DFT calculations result in the frequencies and intensities of the normal modes of the considered species. To bring these frequencies in better agreement with experimental values, we applied a scale factor of 0.951, similar to the value used for many species in the NASA Ames PAH database (Bauschlicher et al. 2010a; Boersma et al. 2014, see e.g.). Generally, these cannot be used to directly compare to astronomical spectra. As mentioned before, the excitation of PAHs in an astronomical context is through single-photon excitation followed by fluorescent emission of IR photons that cools the molecule (see e.g. Allamandola et al. 1989; Bakes & Tielens 1994; Bakes et al. 2001a,b). A realistic model spectrum for an astronomical PAH would thus require detailed knowledge of the frequencies and intensities of all transitions arising from vibrationally excited states, in addition to the anharmonic couplings between the modes. In practice, this information is not readily available for each individual PAH species, and thus several approximations need



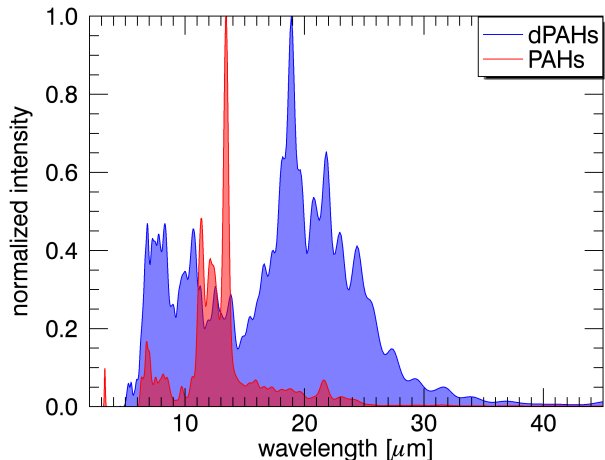


FIG. 5.— The average spectrum of all PAHs in our database (red) compared to the average spectrum of all dPAHs (blue).

to be made. One such approximation is to use the *thermal approximation* (see e.g. d’Hendecourt et al. 1989) in which the state of the molecule is described by its internal “temperature” – the average energy per vibrational mode. At any given temperature, the IR emission scales with a Planck function at that temperature; in essence, a full fluorescence calculation then follows the evolution of the internal temperature and the corresponding emission over the different IR active modes. Such calculations thus provide the scale factors that have to be applied to the different band intensities to account for how much time is spent at what temperature. One then furthermore has to assume a line profile for each of the transitions to obtain a full IR spectrum (for a full description of such models, see the Appendix in Boersma et al. 2014).

A full cascade IR model calculation of the spectra of PAHs and dPAHs would certainly also be the best for our purposes here. However, such calculations are computationally expensive given the large number of species in our database. Moreover, since our main purpose is to find characteristic spectral feature for dPAHs, we are less concerned with relative intensities than with peak positions. Thus, we followed instead a much simpler approach and scaled the intensities by multiplying them with a blackbody of a fixed temperature of 500 K. This corresponds to the assumption that the full fluorescence cascade can be reproduced by a single “characteristic” temperature, and that that temperature is the same for all species. The latter assumption most certainly does not hold: indeed, smaller PAHs have less vibrational modes and thus a higher temperature (energy per mode) for a given UV absorption than larger PAHs. Thus, our approach will somewhat underestimate the emission of smaller PAHs at short wavelengths. For our purposes here, we are mainly interested in the frequencies of the features rather than their intensities; therefore, this is an acceptable default. A gaussian profile with a linewidth of  $5\text{cm}^{-1}$  was chosen.

#### 4.2. Spectral characteristics of dPAHs

We now turn our attention to investigating the typical spectral features of dPAHs. To characterize the features that distinguish a typical dPAH spectrum from a PAH spectrum, we first produced the average spectrum

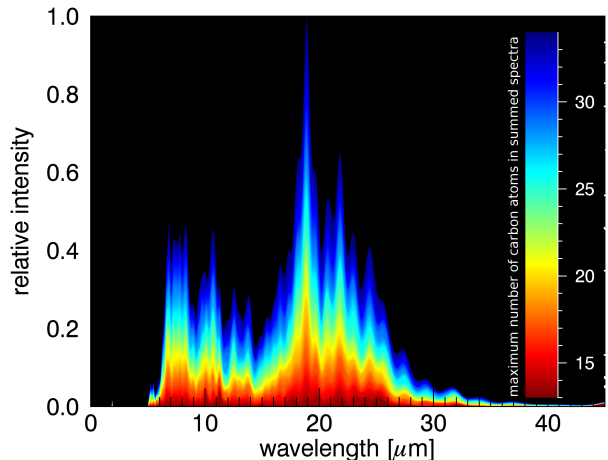


FIG. 6.— Cumulative spectra of dPAHs as a function of size. At the bottom are the spectra of the smallest species (color coded red); we cumulatively added the spectra of ever larger species and changed the color to blue. Careful analysis of the features in this plot can discriminate between features that are common to all dPAHs and features that originate mainly from smaller or larger species.

(arithmetic mean) of all PAHs and that of all dPAHs, and visually compared them for any features of interest (see Fig. 5). To further distinguish how size might influence spectral features, we also produced color-coded cumulative spectra in Fig. 6.

From a close comparison of the average PAH and dPAH spectra, we find notable dPAH features at  $5.2\mu\text{m}$ ,  $5.5\mu\text{m}$ , and  $10.6\mu\text{m}$ , as well as a broad, structured emission forest from  $\sim 16\text{--}30\mu\text{m}$  with its strongest feature at  $19\mu\text{m}$ . These features are absent in the average PAH spectrum, and are thus a first indication that they may represent diagnostic features to recognize a population of dPAHs in astronomical spectra. Our findings compare well to the results by Bauschlicher & Ricca (2013) who also found a  $5.25\mu\text{m}$  feature and emission in the  $15\text{--}25\mu\text{m}$  region they attribute to neutral (large) dPAHs.

It is interesting to note that features of the forest (i.e. emission between  $15\text{--}30\mu\text{m}$ ) appear to follow a broad, somewhat gaussian-like distribution centered around  $20\mu\text{m}$ . Note however that individual species do not show this distribution but have a small number of discrete bands. From Fig. 6 it can be seen that as larger species are added to the average spectrum, some of the features in this forest grow in prominence and are not washed out. This suggests that even some of the features in this forest may have diagnostic power. Another interesting point is that the strongest feature of the forest is at  $19\mu\text{m}$ ; from Fig. 6, it furthermore appears that this feature becomes more prominent than the other forest features for the larger dPAHs. In recent years, emission at this wavelength in astronomical observations has been attributed to fullerenes, but our work shows that a feature at that wavelength may also be due to a family of dPAH-like species.

One could argue that the average dPAH spectrum from our database may not be a good representation of what could be expected in space. Indeed, physical conditions may favour a subclass of species with spectral properties that are somewhat different from the average. Thus,

it may be more appropriate to consider as a diagnostic the transitions that are *most common* among species, i.e. that occur most frequently in our database. We thus studied the transition recurrence by creating histograms of the fraction of species with a transition at a given wavelength. We did this for both PAH and dPAH species, and used a bin size of  $0.1\mu\text{m}$ . To distinguish between weak and strong transitions, we further applied three different intensity cut-offs to our list of transitions before creating the histogram. The three histograms we thus obtained for PAHs and dPAHs are shown in Fig. 7.

The top histogram in Fig. 7 represents essentially no cut off and shows that both PAHs and dPAHs have frequent transitions over the entire wavelength range. There are three clear differences overall between PAHs and dPAHs: (i) all PAHs have a transition at  $3.3\mu\text{m}$  corresponding to the C-H stretching mode; understandably, none of the dPAHs shows this transition. (ii) dPAHs show transitions around  $5.5\mu\text{m}$  where none of the PAHs have transitions. In fact, it turns out that *all* of the dPAH species have at least one transition near  $5.5\mu\text{m}$ . (iii) dPAHs have many more transitions at the longer wavelengths; this is notable from about  $16\mu\text{m}$  onward.

When removing the weakest transitions from the database by increasing the intensity cut-off (middle histogram), these differences between PAHs and dPAHs remain and the long-wavelength dPAH transitions are even more pronounced. Additionally, two clear regions become apparent where many dPAHs have medium or strong transitions, but the regular PAHs don't: an emission feature at  $10.6\mu\text{m}$  and a second one at  $19\mu\text{m}$ . Keeping only the strongest transitions (bottom histogram) we find a histogram that is very similar to the average dPAH spectrum in Fig. 5, but not so for the PAHs. The regions of the typical dPAH spectra that were shown earlier to stand out from a typical PAH spectra also remain present.

Thus, both from a comparison of the average PAH and dPAH spectra, and from the histogram analysis we reach the same conclusion: we would expect that a population of (small) dPAHs would be spectroscopically detectable by their features at  $5.5\mu\text{m}$ ,  $10.6\mu\text{m}$ ,  $19\mu\text{m}$  and a continuum-like 'forest' of individual features roughly between  $16\text{--}30\mu\text{m}$ .

#### 4.3. Correlation analysis

We also addressed the question how "characteristic" the average dPAH spectrum is. To this end, we calculated the linear Pearson correlation coefficient between each of the individual PAH spectra and the average PAH and dPAH spectra, and a similar exercise was carried out for the individual dPAH spectra. We calculated the correlation coefficient over the range  $5\text{--}20\mu\text{m}$  in order to exclude some of the most obvious differences (such as the  $3.3\mu\text{m}$  PAH feature and much of the  $16\text{--}30\mu\text{m}$  dPAH features). The resulting correlation coefficients are shown in Fig. 8.

We found that generally, individual PAH spectra correlate rather well with the average PAH spectrum with an average correlation coefficient of 0.74, with only a fairly modest spread (the majority lies between 0.6 and 0.95). Thus, most individual PAH spectra look fairly similar. This is not so for the dPAH spectra with an average cor-

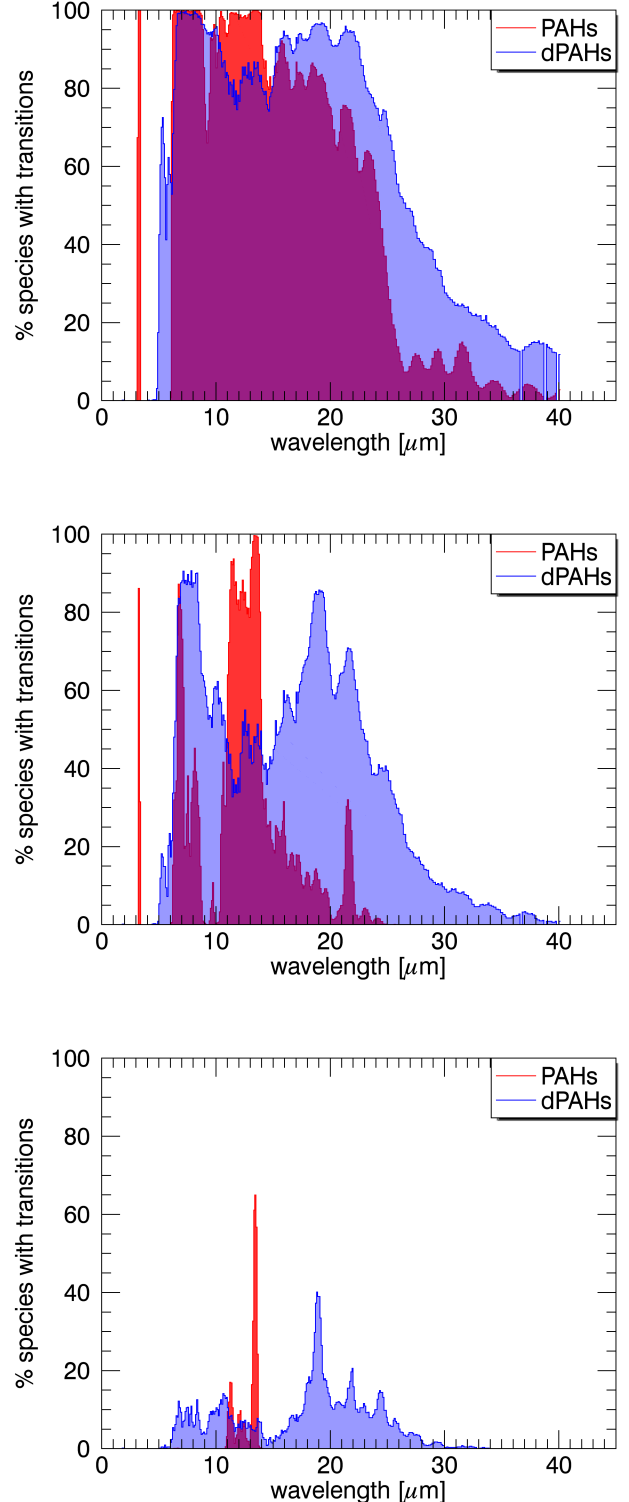


FIG. 7.— Histograms representing the occurrence frequency of transition for PAHs and dPAHs in our database. (*top*) All transitions – essentially no intensity cut-off is applied. (*middle*) Medium and strong transitions only. (*bottom*) Strong transitions only.

relation coefficient of only 0.37 between the individual dPAH spectra and the average dPAH spectrum. Moreover, there is a much larger spread (with most dPAHs having a correlation coefficient roughly between 0.2 and

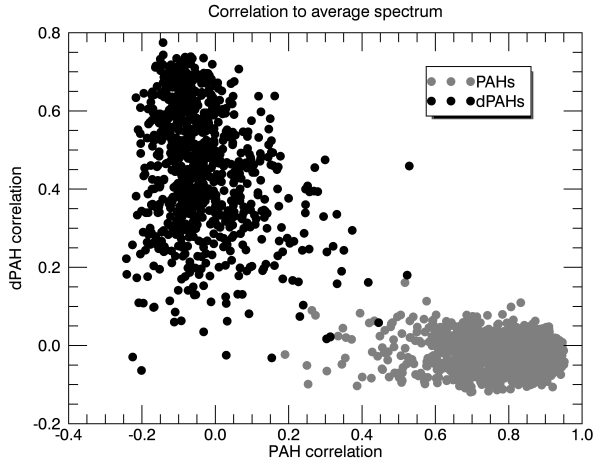


FIG. 8.— The linear Pearson correlation coefficients of individual PAH (gray) and dPAH (black) spectra with respectively the average PAH spectrum (horizontal axis) and average dPAH spectrum (vertical axis).

0.75). Thus, dPAH spectra tend to be much more different from one species to the next. Consequently, it is much harder to “characterize” a typical dPAH spectrum. Referring back to the molecular structures of PAHs and dPAHs this difference can be attributed to the fact that while PAHs tend to be constructed of hexagons that deviate very little from each other, dPAHs are constructed of deformed hexagons that differ greatly from one species to the next, as well as internally to a given species. This effect is most prominent in the lower energy transitions, and is likely the cause of the  $16\text{--}30\mu\text{m}$  continuum. It was found that each species has an almost unique signature in this region. But clearly, these deformations leave their mark in the C-C stretch region as well. These features could provide clues as to which species are present in space, and possibly lead to a detection of a single species. The dPAH and PAH spectra created for this paper will soon be available in the NASA AMES PAH database for others to make use of.

Finally, we considered the correlations between individual PAH spectra and the average dPAH spectra, and vice versa. It is immediately clear from Fig. 8 that the two groups of spectra are very different. Indeed, the correlation plot clearly shows two clusters: one corresponds to the PAH spectra; the other to the dPAH spectra. None of the PAH spectra correlates well with the average dPAH spectrum, and similarly none of the dPAHs correlates well with the average PAH spectrum. Thus, PAHs and dPAHs are spectroscopically very distinct!

We carried out a similar analysis for the other subclasses in table 3; however, we could not find any significant spectroscopic diagnostic for any of those other subclasses.

##### 5. A SEARCH FOR INTERSTELLAR DPAHS

Our analysis above suggests that if a population of dPAHs is present in interstellar environments, we might be able to detect their characteristic spectral features near  $5.5\mu\text{m}$ ,  $10.6\mu\text{m}$  and  $19\mu\text{m}$ , and as structured continuum emission at longer wavelengths. It is very difficult in the best case to establish the latter type of emission.

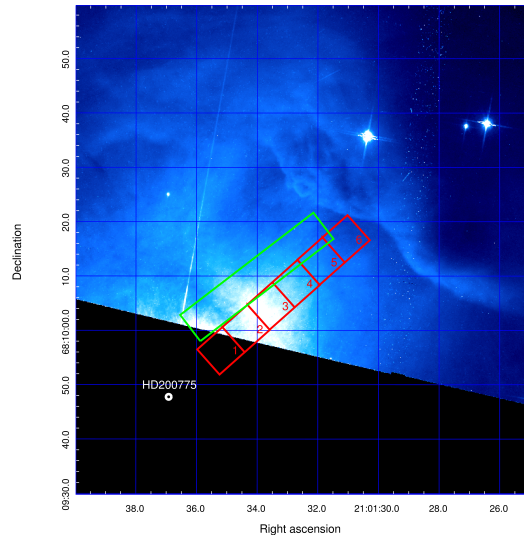


FIG. 9.— A HST image of NGC7023 with the apertures used in this paper (red boxes) and the extraction region used by Berné & Tielens (2012). The illuminating star, HD200775, is indicated by a circle.

At the same time, a feature at  $19\mu\text{m}$  could also be due to fullerenes. At the shorter wavelengths, PAH features are known at  $5.25$  and  $5.7\mu\text{m}$  and those have been attributed to combination bands (Boersma et al. 2009). Thus, it seems that the feature near  $10.6\mu\text{m}$  might offer the best prospects to search for dPAHs. Note however that also here, there might be some confusion since Berné et al. (2013) recently reported a feature at  $10.53\mu\text{m}$  (with a FWHM of  $0.11\mu\text{m}$ ) in a spectrum of NGC 7023 that they attribute to emission of  $\text{C}_{60}^+$ .

NGC 7023 is in fact an ideal object to search for dPAH features for a variety of reasons. A large amount of high-quality IR observations is available for this object (see below), and these data have already been studied in detail in terms of PAHs and fullerenes (see e.g. Sellgren et al. 2007, 2010; Berné & Tielens 2012; Berné et al. 2013; Boersma et al. 2013). Of particular interest here is the work by Berné & Tielens (2012) who studied variations in the IR spectra as one moves from the PDR to regions much closer to the illuminating star HD 200775. In the PDR, far away from the star, the spectrum shows very strong emission from PAHs and no evidence for fullerenes. Approaching the central star though, Berné & Tielens (2012) find that the abundance of PAHs decreases, while that of  $\text{C}_{60}$  increases. They argue that fullerenes form from large PAHs ( $\sim 70$  C atoms) that become dehydrogenated by UV radiation, subsequently close up and shrink down to become  $\text{C}_{60}$ . Thus, large dPAHs are explicitly suggested as an intermediate step in the formation of fullerenes. However, smaller PAHs could also become fully dehydrogenated at even lower doses of UV radiation. Thus, dPAHs may be formed over a much larger area than only between the PAHs and the fullerenes. If enough of these dPAHs survive for long enough, they might be detectable.

A large amount of IR spectroscopic observations of NGC 7023 were carried out by the IRS spectrograph (Houck et al. 2004) on board the Spitzer Space Tele-



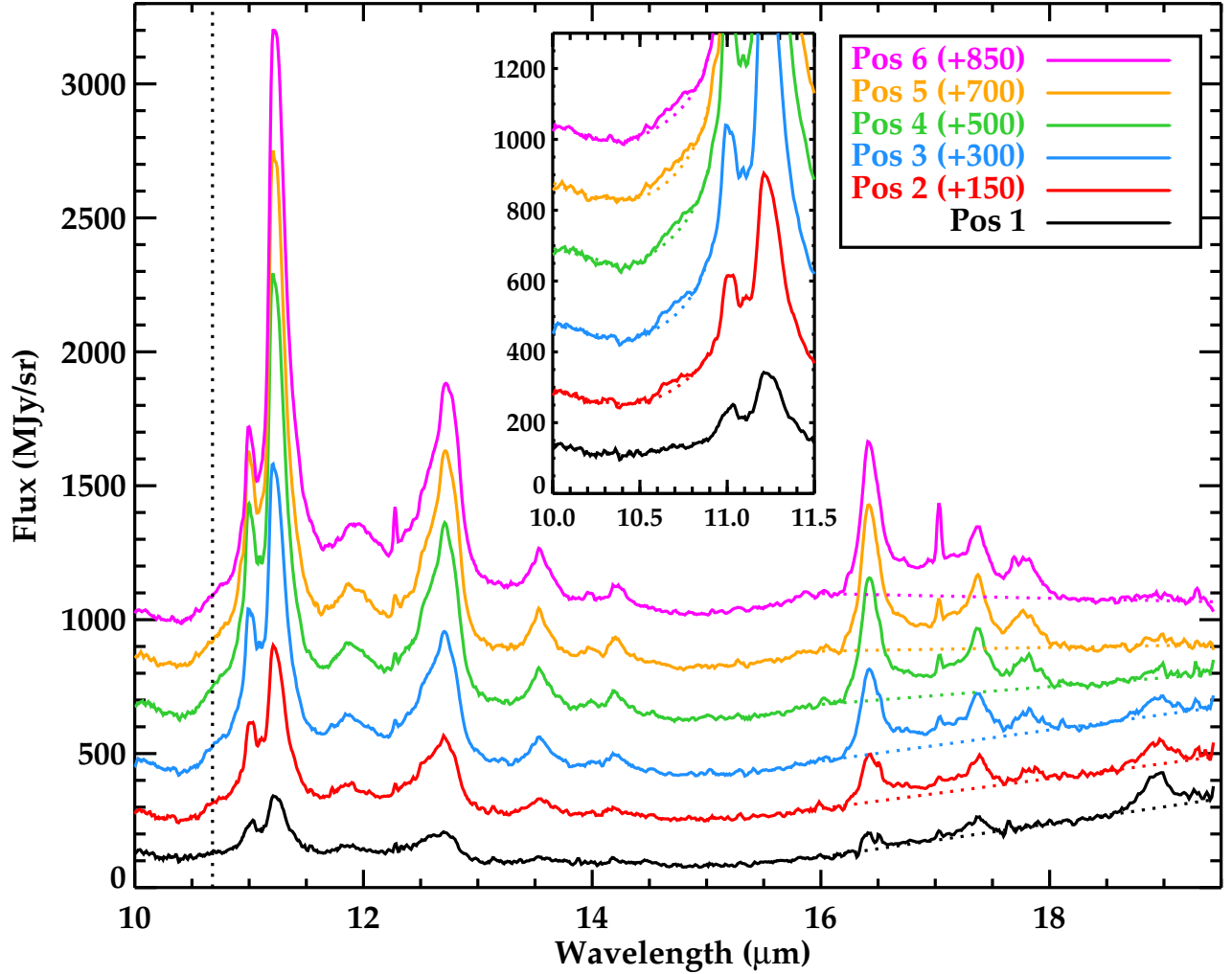


FIG. 10.— The six Spitzer-IRS SH spectra for NGC 7023 as a function of increasing distance to the illuminating star, corresponding to the apertures shown in Fig. 9. We smoothed the spectra with a 3 pixel wide boxcar average and we have offset them for clarity using the offsets indicated in the legend. The dotted lines redward of  $16\mu\text{m}$  are least absolute deviation fits to the local continuum for each spectrum. The dotted line at  $10.68\mu\text{m}$  marks the center of a very weak emission feature (best seen in positions 2 and 3) in the wing of the  $11.0\mu\text{m}$  PAH band. The inset shows a close-up of this wavelength range, where the dotted lines now represent a spline fit through the wing of the  $11.0\mu\text{m}$  PAH band, used to extract the much weaker  $10.68\mu\text{m}$  feature (see text for details).

scope (Werner et al. 2004). Here, we use primarily the high-resolution spectra taken with the Short-High (SH) module covering the wavelength range  $10\text{--}19\mu\text{m}$  at a resolving power of  $R \sim 600$  (AOR 3871232). We will also include some discussion about the low-resolution spectra taken with the Short-Low (SL) module covering the wavelength range  $5.2\text{--}14\mu\text{m}$  (AORs 3871488 and 3871744). We did not apply background subtraction. We cleaned the data using *cubism*'s automatic bad pixel generation with  $\sigma_{\text{TRIM}} = 7$  and Minbad-fraction = 0.5 and 0.75 for the global bad pixels and record bad pixels. We have extracted spectra corresponding to 6 different positions throughout the nebula at increasing distances from the illuminating star (see Fig. 9). The chosen positions are comparable to those by Berné & Tielens (2012, their extraction regions are also shown in Fig. 9).

The full  $10\text{--}19\mu\text{m}$  spectra (Fig. 10) reveal the same overall spectral variations that were described by Berné & Tielens (2012): strongest PAH emission in position 6

(furthest away from the illuminating star), and gradually less PAHs and more fullerenes ( $17.4\mu\text{m}$  and  $18.9\mu\text{m}$  bands) toward position 1. Close inspection of this figure reveals a very weak feature near the predicted wavelength of  $10.6\mu\text{m}$  (centered at  $10.68\mu\text{m}$ , indicated with the dotted line), most clearly seen in the spectra corresponding to positions 2 and 3. To extract this feature, we need to somehow estimate the “local continuum”, i.e. the underlying contribution of the wing of the  $11.0\mu\text{m}$  feature. To do so, we first defined a set of 7 anchor points in the spectrum of position 2 between  $10.0$  and  $10.95\mu\text{m}$ , but excluding the range  $10.5\text{--}10.8\mu\text{m}$  where the feature is located. A cubic spline through these anchor points then represents an estimate of the local continuum. We then fixed the wavelengths of these anchor points but iteratively allowed their flux values to vary to find the cubic spline that provides the best fit to the spectrum in this range (but still excluding the  $10.5\text{--}10.8\mu\text{m}$  range). We then did the same for the remaining positions, always us-

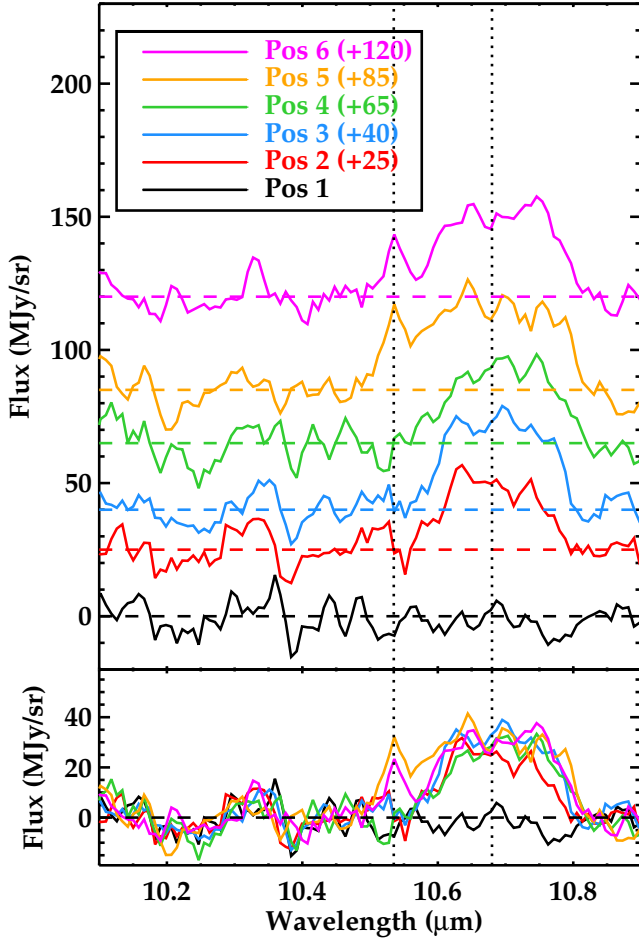


FIG. 11.— The spectra of NGC 7023 (smoothed as in Fig. 10, and offset) after subtracting the cubic spline fit to represent the wing of the  $11.0\mu\text{m}$  feature (dotted line in the inset of Fig. 10). The feature centered at  $10.68\mu\text{m}$  (indicated by the right dotted line) is clearly present in positions 2–6, but absent in position 1. An additional, much narrower emission feature centered at  $10.53\mu\text{m}$  (indicated by the left dotted line) appears in positions 5 and 6. The dashed lines indicate the zero-point level for each spectrum.

ing the same 7 fixed wavelengths as anchor points. The resulting curves are shown as dotted lines in the inset of Fig. 10. They are smooth, contain no spectral structure, and seem to correspond well to what might be the wing of the  $11.0\mu\text{m}$  feature. We are thus confident that this is a reasonable approximation to the spectrum under the weak  $10.68\mu\text{m}$  feature. However, we realize that there is a fair amount of uncertainty in this determination.

Fig. 11 shows the resulting  $10.1\text{--}10.9\mu\text{m}$  spectra after subtraction of this local continuum. The feature at  $10.68\mu\text{m}$  is now very clearly visible in the spectra of positions 2–6, but absent in position 1. It is also interesting to note that in positions 5 and 6, an additional, even weaker emission feature is superposed on the spectrum, with a central wavelength of  $10.53\mu\text{m}$ . This coincides with the reported wavelength of a weak feature (with a peak height of  $\sim 6 \text{ MJy sr}^{-1}$ ) that was associated with  $\text{C}_{60}^+$  by Berné et al. (2013) in a spectrum of NGC 7023 very close to the central star. We do not find evidence for such a feature in our position 1 spectrum (where we would expect it) but surprisingly at the positions furthest

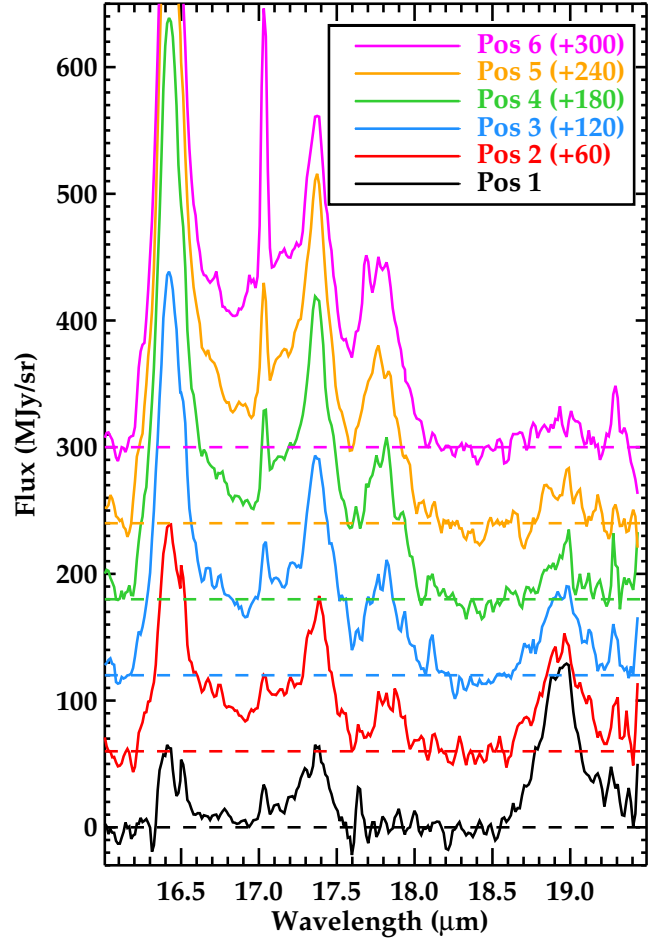


FIG. 12.— The spectra of NGC 7023 (smoothed as in Fig. 10, and offset) after subtracting the linear fit to the continuum (the dotted lines in Fig. 10). The dashed lines indicate the zero-point level for each spectrum.

away from the star, and much stronger than the feature reported by Berné et al. (2013). It is also slightly narrower than the reported  $\text{C}_{60}^+$  feature. Where the  $10.68\mu\text{m}$  feature is present, it appears roughly the same in terms of width, shape and overall (absolute) strength. In contrast, the intensity of the PAH emission increases by about a factor of 10 between positions 1 and 6 (see Fig. 10). The width of the feature (FWHM of about  $0.2\mu\text{m}$ ) is comparable to e.g. the  $11.2$  or  $16.4\mu\text{m}$  PAH features. It is thus possible that the  $10.68\mu\text{m}$  is indeed the weak emission of a population of dPAHs.

If dPAHs are responsible for the  $10.68\mu\text{m}$  feature, they should also emit at other wavelengths. We first considered the  $19\mu\text{m}$  region. It is clear from Fig. 10 that a well-defined emission band is present in the spectra of positions 1–3; there is a hint though of weaker emission in the other positions as well. To better evaluate this possibility, we fitted a least-absolute-deviation straight line to the continuum longward of  $16\mu\text{m}$ , excluding the wavelength ranges of PAH and  $\text{C}_{60}$  features (see Fig. 10). While this may not be the best possible representation of the local continuum, it ensures that we do not introduce any artificial features in the spectrum. Fig. 12 shows the resulting continuum-subtracted spectra in this wave-

length range. This figure now more convincingly shows that weak excess emission at  $19\mu\text{m}$  also appears at the other positions. While a  $19\mu\text{m}$  feature could be due to  $\text{C}_{60}$ , this is not likely the case for the emission we see at all positions in NGC 7023. Indeed, if the emission at  $19\mu\text{m}$  is due to  $\text{C}_{60}$ , there should also be associated features at  $7.0$ ,  $8.6$  and  $17.4\mu\text{m}$ . Unfortunately, there is severe blending with other PAH features, most notably the strong  $8.6\mu\text{m}$  and the  $17.4\mu\text{m}$  PAH bands. However, from inspecting the SL spectra, we can clearly see the  $7.0\mu\text{m}$   $\text{C}_{60}$  feature in the wing of the  $7.7\mu\text{m}$  PAH band at position 1, and weakly also in position 2; not in the other positions. It may thus well be that some of the  $19\mu\text{m}$  emission we see is due to dPAHs. Finally, we also studied the SL data around the  $5.5\mu\text{m}$  region. We did not find evidence for an emission feature at  $5.5\mu\text{m}$  – if any, they would be even weaker than the already fairly weak  $5.25$  and  $5.7\mu\text{m}$  PAH bands. This is in line with expectations though: also in our average spectrum, the  $5.5\mu\text{m}$  band is a few times weaker than the  $10.6\mu\text{m}$  band (see Fig. 5).

## 6. DISCUSSION

Several authors have presented detailed theoretical studies on hydrogenation and dehydrogenation of interstellar PAHs (Allain et al. 1996; Vuong & Foing 2000; Le Page et al. 2001; Montillaud et al. 2013). These studies show that interstellar PAHs are generally either fully hydrogenated, or fully dehydrogenated; intermediate hydrogenation states can only exist over a very small range in physical conditions (typically measured by  $n_{\text{H}}/G_0$ ). This is a consequence of the fact that more dehydrogenated PAHs are less photostable; thus, once the first H atom is removed, it becomes easier to remove the next. The hydrogenation balance furthermore also depends critically on the size of the PAHs. Indeed, larger PAHs are less susceptible to H loss than smaller PAHs since they can more easily dissipate the absorbed UV energy. Thus, given the physical conditions, there is a critical PAH size: PAHs smaller than this critical size will be rapidly stripped of their hydrogen atoms; larger PAHs will remain fully hydrogenated. There may be some discussion about where precisely this size limit is. For NGC 7023 for instance, Berné & Tielens (2012) find a critical size of about 60 carbon atoms in the PDR where PAH emission dominates, and about 70 carbon atoms closer to the star where  $\text{C}_{60}$  is located. However, Montillaud et al. (2013) find that even in the PDR (of NGC 7023), these PAHs are fully dehydrogenated.

There is thus little doubt that a considerable amount of PAH molecules becomes fully dehydrogenated in interstellar environments. However, these dPAHs are then expected to further undergo photodissociation, fragmentation, and isomerization. Thus, it is not expected that a large population of dPAHs could exist in the interstellar medium. Also Mallocci et al. (2008) concluded that there can only be at most a small population of fully dehydrogenated species in the ISM since dPAHs would otherwise leave a clear imprint on the UV extinction curve.

If the emission at  $10.68\mu\text{m}$  and  $19\mu\text{m}$  that we observe in NGC 7023 is indeed due to dPAHs, it implies that

there is a small, but observable population of fully dehydrogenated PAH molecules in these environments. This could reflect that dPAHs survive just long enough, or alternatively could point to a subpopulation of dPAHs that are more hardy and withstand radiation more easily than others. It is puzzling though that the strength of the  $10.68\mu\text{m}$  feature is so constant from position 2 to position 6 while the PAH bands at the same time change in intensity by a factor of 10. It appears as if the changing physical conditions ( $n_{\text{H}}, G_0$ ) have little to no effect on the emitting population until reaching position 1 where the dPAHs disappear. Most likely this represents the position where even the hardest species photodissociate; alternatively, this is where they isomerize into cages and develop into fullerenes. If this is the case, the fullerenes likely form from smaller cages (since smaller dPAHs at this point are more abundant due to fragmentation) rather than from larger PAHs. Position 1 could then represent the point where the conditions are energetic enough for close network growth (CNG) and isomerization into  $\text{C}_{60}$  to complete.

## 7. SUMMARY & CONCLUSIONS

We have studied the IR spectroscopic properties of fully dehydrogenated PAH molecules. We have created a complete database of fully optimized PAH structures for species with up to eight benzenoid rings, and their fully dehydrogenated counterparts. The majority (64%) of the PAHs and about half of the dPAHs in our database turn out to be non-planar. Upon dehydrogenation, most (71%) dPAHs develop pentagons in their carbon skeleton. We then calculated the frequencies and intensities of the normal modes for all species in our database and analyzed their spectra. We found that dPAHs characteristically exhibit features at  $5.5\mu\text{m}$ ,  $10.6\mu\text{m}$  and  $18.9\mu\text{m}$  in addition to a forest of weaker features in the  $16\text{--}30\mu\text{m}$  range that appear as structured continuum emission. We searched for these features in spectra of the well-studied reflection nebula NGC 7023, corresponding to various positions with changing physical conditions and hence different emission characteristics. We detect weak emission at  $10.68\mu\text{m}$  in 5 out of 6 positions; this emission is furthermore accompanied by emission at  $19\mu\text{m}$  that we see at all positions. We tentatively see this as evidence for a small population of emitting dPAHs in these environments. These emission characteristics disappear closest to the illuminating star, where  $\text{C}_{60}$  has been detected. This suggests that  $\text{C}_{60}$  could indeed form from dPAHs, but it appears more likely that they form from smaller dPAHs rather than from larger species.

We would like to thank Xander Tielens and Lou Allamandola for the stimulating and helpful discussions. We would also like to thank the anonymous referee for the constructive comments. This work was supported by a grant from the Academic Development Fund (ADF) from Western University, and by a Discovery Grant from the Natural Sciences and Engineering Research Council (NSERC). This work was made possible by the facilities of the Shared Hierarchical Academic Research Computing Network (SHARCNET: [www.sharcnet.ca](http://www.sharcnet.ca)) and Compute/Calcul Canada.

## REFERENCES

- Allain T., Leach S., Sedlmayr E., 1996, *A&A* 305, 616
- Allamandola L.J., Hudgins D.M., Sandford S.A., 1999, *ApJ* 511, L115
- Allamandola L.J., Tielens A.G.G.M., Barker J.R., 1985, *ApJ* 290, L25
- Allamandola L.J., Tielens G.G.M., Barker J.R., 1989, *ApJS* 71, 733
- Bakes E.L.O., Tielens A.G.G.M., 1994, *ApJ* 427, 822
- Bakes E.L.O., Tielens A.G.G.M., Bauschlicher, Jr. C.W., 2001a, *ApJ* 556, 501
- Bakes E.L.O., Tielens A.G.G.M., Bauschlicher, Jr. C.W., Hudgins D.M., Allamandola L.J., 2001b, *ApJ* 560, 261
- Bauschlicher, Jr. C.W., Boersma C., Ricca A., et al., 2010, *ApJS* 189, 341
- Bauschlicher C.W., Ricca A., 2010 *Mol. Phys.* 108, 2647
- Bauschlicher C. W., 2014 *Chem. Phys.*, submitted.
- Bauschlicher, Jr. C.W., Ricca A., 2013, *ApJ* 776, 102
- Becke A.D., 1993, *J. Chem. Phys.* 98, 5648
- Berné O., Mulas G., Joblin C., 2013, *A&A* 550, L4
- Berné O., Tielens A.G.G.M., 2012, *Proceedings of the National Academy of Science* 109, 401
- Boersma C., Bauschlicher C. W., Allamandola L. J., et al., 2010, *A&A* 511, A32.
- Boersma C., Bauschlicher, Jr. C.W., Ricca A., et al., 2014, *ApJS* 211, 8
- Boersma C., Bregman J.D., Allamandola L.J., 2013, *ApJ* 769, 117
- Boersma C., Mattioda A.L., Bauschlicher, Jr. C.W., et al., 2009, *ApJ* 690, 1208
- Boersma C., Rubin R.H., Allamandola L.J., 2012, *ApJ* 753, 168
- Cami J., 2011, In: Joblin C., Tielens A.G.G.M. (eds.), *EAS Publications Series*, vol. 46 of *EAS Publications Series*, pp. 117–122
- Cami J., 2013, In: Cami J., Cox N. (eds.), *IAU Symposium*, vol. 297 of *IAU Symposium*, pp. 377–381
- Cami J., Bernard-Salas J., Peeters E., Malek S.E., 2010, *Science* 329, 1180
- Chuvilin A., Kaiser U., Bichoutskaia E., Besley N.A., Khlobystov A.N., 2010, *Nat. Chem.* 2, 450
- d'Hendecourt L., Léger A., Boissel P., Désert F., 1989, In: L. J. Allamandola & A. G. G. M. Tielens (ed.), *Interstellar Dust*, vol. 135 of *IAU Symposium*, pp. 207–+
- Dunk P.W., Adjizian J.J., Kaiser N.K., et al., 2013, *Proceedings of the National Academy of Science* 110, 18081
- Dunk P.W., Kaiser N.K., Hendrickson C., et al., 2012, *Nat. Commun.* 3, 855
- Frisch M.J., Pople J.A., Binkley J.S., 1984, *J. Chem. Phys.* 80, 3265
- Frisch M.J., Trucks G.W., Schlegel H.B., et al., 2009, Gaussian 09 Revision D.01. Gaussian Inc. Wallingford CT 2009
- García-Hernández D.A., Iglesias-Groth S., Acosta-Pulido J.A., et al., 2011a, *ApJ Lett.* 737, L30+
- García-Hernández D.A., Kameswara Rao N., Lambert D.L., 2011b, *ApJ* 729, 126
- García-Hernández D.A., Manchado A., García-Lario P., et al., 2010, *ApJ Lett.* 724, L39
- Gielen C., Cami J., Bouwman J., Peeters E., Min M., 2011, *A&A* 536, A54
- Hony S., Van Kerckhoven C., Peeters E., et al., 2001, *A&A* 370, 1030
- Houck J.R., Roellig T.L., van Cleve J., et al., 2004, *ApJS* 154, 18
- Hudgins D.M., Bauschlicher, Jr. C.W., Allamandola L.J., 2005, *ApJ* 632, 316
- Jäger C., Huiskens F., Mutschke H., Jansa I.L., Henning T., 2009, *ApJ* 696, 706
- Kroto H.W., Heath J.R., O'Brien S.C., Curl R.F., Smalley R.E., 1985, *Nat* 318, 162
- Le Page V., Snow T.P., Bierbaum V.M., 2001, *ApJS* 132, 233
- Lee C., Yang W., Parr R.G., 1988 *Phys. Rev. B* 2, 785
- Leger A., Puget J.L., 1984, *A&A* 137, L5
- Mallocci G., Mulas G., Cecchi-Pestellini C., Joblin C., 2008, *A&A* 489, 1183
- Micelotta E.R., Jones A.P., Cami J., et al., 2012, *ApJ* 761, 35
- Montillaud J., Joblin C., Toubanc D., 2013, *A&A* 552, A15
- Nikolić S., Trinajstić N., Knop J., Müller W., Szymanski K., 1990, *Journal of Mathematical Chemistry* 4, 357
- Otsuka M., Kemper F., Cami J., Peeters E., Bernard-Salas J., 2013a, *MNRAS*
- Otsuka M., Kemper F., Hyung S., et al., 2013b, *ApJ* 764, 77
- Peeters E., 2014, In: Cami J., Cox N.L.J. (eds.), *IAU Symposium*, vol. 297 of *IAU Symposium*, pp. 187–196
- Peeters E., Hony S., Van Kerckhoven C., et al., 2002, *A&A* 390, 1089
- Peeters E., Tielens A.G.G.M., Allamandola L.J., Wolfire M.G., 2012, *ApJ* 747, 44
- Roberts K.R.G., Smith K.T., Sarre P.J., 2012, *ArXiv e-prints*
- Rubin R.H., Simpson J.P., O'Dell C.R., et al., 2011, *MNRAS* 410, 1320
- Sellgren K., Uchida K.I., Werner M.W., 2007, *ApJ* 659, 1338
- Sellgren K., Werner M.W., Ingalls J.G., et al., 2010, *ApJ Lett.* 722, L54
- Sloan G.C., Lagadec E., Zijlstra A.A., et al., 2014, *ApJ* 791, 28
- Stephens P. J., Devlin F.J., Chabalowski C.F., Frisch M.J., 1994 *J. Phys. Chem.* 98, 11623
- Tielens A.G.G.M., 2008, *ARA&A* 46, 289
- van Dienenhoven B., Peeters E., Van Kerckhoven C., et al., 2004, *ApJ* 611, 928
- Vuong M.H., Foing B.H., 2000, *A&A* 363, L5
- Werner M.W., Roellig T.L., Low F.J., et al., 2004, *ApJS* 154, 1
- Zhang Y., Kwok S., 2011, *ApJ* 730, 126